Investigation of the characteristics of low-level jets over North America in a convection-permitting WRF simulation

Xiao Ma[1], Yanping Li[1], Zhenhua Li[1], Fei Huo[1]

[1]Western University, 1151 Richmond Street, London, Ontario, Canada, N6A 3K7

Correspondence to: Yanping Li (yli4972@uwo.ca)

Abstract. In this study, we utilized a high-resolution (4 km) convection-permitting Weather Research Forecasting (WRF) simulation spanning a 13-year period (2000-2013) to investigate the climatological features of Low-level Jets (LLJs) over North America. The 4-km simulation enabled us to represent the effects of orography and the underlying surface on the boundary layer winds better. Focusing on the continental US and the adjacent border regions of Canada and Mexico, this study not only identified several well-known large-scale LLJs such as the southerly Great Plains LLJ and the summer northerly California coastal LLJ, but also the winter Quebec northerly LLJ which gets less focus before. All these LLJs reach the strongest in the night time in the diurnal cycle. Thus, the different thermal and dynamic mechanisms forming these three significant LLJs are investigated in this paper: Inertial oscillation theory dominates in Great Plain LLJ, California coastal LLJ is formed by the baroclinic theory, whereas the Quebec LLJ is associated with both theories. Moreover, the high-resolution simulation revealed climatic characteristics of weaker and smaller-scale LLJs or low-level wind maxima in regions with complex terrains, such as the northerly LLJs in the foothill regions of the Rocky Mountains and the Appalachian during the winter. This study provides valuable insights into the climatological features of LLJs in North America and the high-resolution simulation offers a more detailed understanding of LLJ behavior near complex terrains and other smaller-scale features.

1. Introduction

A low-level jet (LLJ) is described as the fast-moving air ribbon located in the lower atmosphere most of the time (Bonner, 1968; Rife et al., 2010). Many of the world's LLJs have been studied, such as the Great Plains LLJ over the central US (Bonner, 1968; Zhong et al., 1996), the Somali LLJ over eastern Africa (Munday et al., 2021), and the South American LLJ over the east Andes Mountains (Montini et al., 2019). Other studies extend beyond in-land LLJs to encompass offshore coastal LLJs such as the California LLJs (Parish, 2000) and North African Coastal LLJ (Soares et al., 2018). A kind of mesoscale weather system, an LLJ has a relatively small vertical range of usually only a few hundred meters, but its width can reach several hundred kilometers. LLJs are closely related to precipitation and even extreme events, and they can transfer abundant water vapor to the downwind regions, providing favorable dynamic conditions for rainfall (Walters and Winkler, 2001; Hodges and Pu, 2019). Meanwhile, researchers have long been interested in investigating their features, because LLJs also affect various processes such as wind power development, air pollution transportation, and urban heat islands: the wind turbines would be influenced by positive wind shear and downward entrainment from the LLJs above them, assisting in extracting energy from the strong wind belt inside LLJs (Gadde and Stevens 2021; Ma et al., 2022). LLJ-related horizontal transportation is beneficial to pollutant removal (Sullivan et al. 2017). The LLJs can enhance the turbulent mixing in the boundary layer thereby decreasing the atmospheric stability, helping pollution diffusion, and weakening urban heat island intensity (Hu et al., 2013).

Since the mid-20th century, scientists have used regular rawinsonde observations to investigate the characteristics of LLJs. Applying rawinsondes to investigate the Great Plains LLJ in the central US, Bonner (1968), Mitchelle et al. (1995), and Walters et al. (2008) studied its distribution, seasonal activity, horizontal and vertical structure, and diurnal features and established the climatology of the Great Plains LLJ during warm seasons. As well as rawinsondes, radar systems and wind profilers are useful tools for characterizing LLJs. Frisch et al. (1992) observed a typical LLJ process using Doppler weather radar in North Dakota and identified that the friction on the surface of the boundary layer is important in the early stages of LLJ development. Using long-term wind profiler measurement, Miao et al. (2018) interpreted the climatology of LLJs in Beijing and Guangzhou, concluding that the frequency values of LLJs in these two cities are 13.0% and 4.9%, respectively. Moreover, Smith et al. (2019) used the Plains Elevated Convection at Night (PECAN) observations to conduct high-quality measurements of nocturnal LLJs with wide spatial and temporal resolutions. They found that sudden changes in LLJ structure typically result from the spatial evolution of the LLJ.

49   However, there are some disadvantages of observational research that should be noted. First, regular rawinsonde data

50   only contain measurements at two daily time points (00 UTC and 12 UTC), which cannot fully capture LLJs' diurnal

51   variations. The time density of observations is therefore coarse, and coastal areas lack regular high-density

52   measurements, making the study of coastal LLJs challenging (Mitchell et al., 1995). Second, heterogeneities in the

53   rawinsonde records, such as variations in station locations, radiosonde types, and archiving procedures, may also

54   complicate the use of these observations in climate research. Third, rawinsonde measurements taken at a single point

55   are not able to capture horizontal shear and environmental conditions (Chen et al., 2005). Although observation

56   platforms such as radar, PECAN, or lidar which investigate the atmosphere as low as 300 m, can compensate to some

57   extent for this lack of observational data. as well as lidar that investigates the atmosphere as low as 300 m, these

58   approaches are still limited by the spatial coverage of their measurement platforms (Smith et al., 2019).

59   Because of these problems with observational methods, researchers have chosen reanalysis datasets as an alternative

60   for investigating LLJs. Reanalysis data have relatively better spatial and temporal coverage than rawinsonde

61   measurements, incorporate observations into the preliminary model simulations, provide more comprehensive

62   variables through assimilation, and contain broader domains. Rife et al. (2010) highlighted the global distribution of

63   identified nocturnal LLJs using reanalysis data with a horizontal grid spacing of 40 km, and even successfully

64   extracted some previously unknown jets, like Tarim nocturnal LLJ in northwest China, Ethiopia nocturnal LLJ, and

65   Namibia–Angola nocturnal LLJ. Doubler et al. (2015) applied the North American Regional Reanalysis (NARR)

66   dataset (~32 km) to generate long-term LLJ climatology in North America. Consistent with previous records,

67   Doubler's results supplemented the description of some smaller-scale LLJs. Similarly, Montini et al. (2019) compared

68   and validated the performance of five different reanalysis datasets in identifying LLJs. Their results showed the 38-

69   year climatology of South American LLJs with ERA-Interim data (~79 km).

70   Scientists have also conducted studies based on numerical simulations, which can more accurately represent LLJs than

71   reanalysis data sets, especially in the vertical direction, thereby yielding new insights into LLJs' features. Tang et al.

72   (2017) used an ensemble of dynamically downscaling regional climate simulations to generate the climatology of

73   Great Plains LLJ and predicted that the LLJ will occur more frequently during the nighttime in spring and summer in

74   mid-21st century. Jiménez-Sánchez et al. (2019) conducted a simulation for LLJs over the Orinoco River Basin by

75   dynamic downscaling of the Weather Research and Forecasting model (WRF). The simulation represented the jet

streaks better than previous studies within a broader region of wind enhancement and illustrated more detailed diurnal evolution. Nevertheless, most general numerical simulations still represent the convective processes by the parameterization scheme, which generates uncertainty in the results. These issues can be addressed by using convection-permitting models with grid spacing under 5 km that adequately simulate the convections and other small-scale processes (Liu et al., 2017, Li et al., 2019, Kurkute et al., 2020). Convection-permitting modeling describes the underlying surface more accurately than coarse-resolution simulations and reanalysis data and shows ability in investigations of LLJs near complex mountain areas. Du and Chen (2019) analyzed the LLJs over southern China by using 4-km WRF model and revealed a solid relationship between the mesoscale lifting of LLJs and the convection's initiation. They also highlighted the importance of coastal terrain. Overall, the finer-resolution tools tend to show more comprehensive and precise results, offering detailed and accurate references to LLJs.

The formation mechanisms of LLJs have been studied extensively by researchers. In explaining the diurnal cycle feature of the Great Plains LLJ, the inertial oscillation theory proposed by Blackadar (1957) and Stensrud (1996) suggests that the LLJ is related to the friction change in the boundary layer. During the night, the jet-core wind is enhanced after decoupling with near-surface friction. Holton (1967) and Parish (2000) developed the thermal wind adjustment theory, which suggests that the horizontal pressure gradient changes because the atmosphere over sloping terrain is warmer or because sea-land contrast influences the diurnal cycle of wind. Additionally, LLJs can also be formed due to synoptic system forcing, as proposed by Uccellini et al. (1987) and Saulo et al. (2007). However, convection-permitting models can help explain how LLJs form because they have precise descriptions of weather systems and underlying orography. Using 4-km simulations, Fu et al. (2018) and Zhang et al. (2019) analyzed the evolution of LLJs over mountainous areas in eastern and southwestern China, respectively. They concluded that inertial oscillation plays a prominent role in and is responsible for the local precipitation peak at a certain time. Besides, Shapiro et al. (2016) argued that the formation of some LLJs may not be impacted by a single factor and that a unified theory analysis is thus required. Thus, a dataset that offers more information must be very popular. All these studies have shown that convection-permitting models, with both finer coverage and resolutions, are a powerful tool for LLJ characteristics research.

In this study, we utilize the 4-km convection-permitting WRF simulation (Liu et al., 2017) to analyze the features of low-level jet systems across North America, improving the spatial and temporal resolutions. Section 2 introduces the

103 model configuration and the criteria for LLJ identification, Section 3 presents the characteristics of LLJ frequencies

104 in North America, and Section 4 illustrates the analysis of the background and mechanisms in several LLJ cases.

105 Finally, Section 5 provides the discussion and conclusion.

106 **2. Model configuration and methods**

107 **2.1 WRF setup**

108 This study utilized a convection-permitting Weather Research and Forecasting (WRF) dataset (Liu et al. 2017, Data

109 available at: https://rda.ucar.edu/datasets/ds612.0/) with a horizontal resolution of 4 km over North America, without

110 nesting. The domain covers the entire continental US, Southern Canada, and Northern Mexico, as illustrated in Figure

111 1. The simulation provides three-dimensional data at a temporal resolution of 3 hours, resulting in 8-time steps per

112 day. In the vertical direction, the data have 51 eta levels and can reach 50 hPa. It should be noted that there are five

113 layers under 500-m height and nine layers under 1 km are outputted above ground level, which means the WRF has a

114 better ability than other coarse modelling, to capture the LLJs occurring in the boundary layer. Considering the

115 computational cost for high-resolution modelling, this simulation period spans from 1st October 2000 to 30th

116 September 2013, and the six-hourly ERA-Interim reanalysis dataset of 0.7° resolution was used as input for the climate

117 simulation, the vertical layer depth of the forcing ERA-Interim data under 5 km is about 0.3-1.4 km (Hoffmann &

118 Spang, 2022). Even though the version is older, the ERA-Interim dataset still has been maturely applied in the climate

119 modelling study and accumulating a wealth of related cases and experiences (Liu et al., 2017, Li et al., 2019). Besides,

120 it is noted that 13 years is shorter than the normally defined climatology, but considering the computational cost of

121 high-resolution simulation, it is still a balanced compromise. This shorter period length was also utilized to analyze

122 the climate features of other weather events (Liu et al., 2017, Ma et al., 2022). The simulation did not apply any

123 cumulus parameterization scheme due to the fine horizontal grid spacing, but other sub-grid scale processes were

124 parameterized by various physical schemes: the rapid radiative transfer model (RRTMG) (Iacono et al., 2008) was

125 used for simulating longwave and shortwave radiations, the Yonsei University (YSU) scheme was used for

126 representing the planetary boundary layer (Hong et al., 2006), and the Noah-MP model was used for computing surface

127 processes (Niu et al., 2011). In this study, the planetary boundary layer scheme is retained. Nonetheless, it should be

128   noted that this would introduce uncertainties to the simulation in the vertical direction, especially in regions with

129   complex topography.
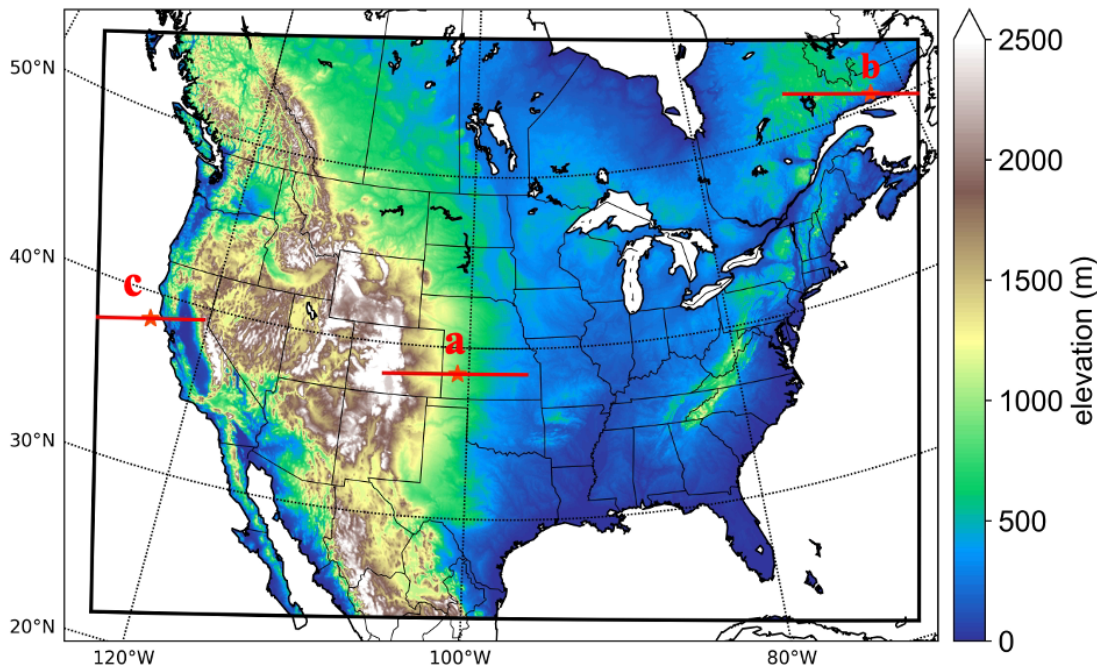
130
131   **Figure 1. Study domain of this convection-permitting model. The colors represent the elevation. The red lines and stars**
132   **show the positions of investigated cross-section and jets in Section 4.**

133

134   **2.2 Methodology**

135   Using the threshold criteria proposed by Bonner (1968), this study identifies LLJs from the vertical wind profile of

136   each grid point in the model output data. LLJs are present when the following conditions are met: (1) the height of the

137   LLJ core maximum wind speed is below 3 km above the ground level (AGL); (2) the maximum wind speed is greater

138   than or equal to 12 m s-1; (3) from the height of the wind maxima to the height of the next minimum value or 3-km

139   height (whichever is lower), the velocity of winds drop by at least 6 m s-1; (4) the wind speed drops by at least 6 m s-

140   1 below the level of wind maxima. On the other hand, the investigation of LLJs is normally conducted with different

141   jet-core wind directions. Pu and Cook (2010) studied the West African Westerly Jet, this zonal LLJ can help transport

142   water vapor from the Atlantic to Africa, this LLJ is related to the westward extension of the continental thermal low

143   pressure over Africa in summer. Thus, the LLJ research should refer to the local climatologic or geographic features.

144   Considering the importance of the meridional LLJ for heat and water vapor transport over North America, as well as

145   the direction of the Rockies, this study addresses LLJ frequencies in different meridional directions. According to

146   Walter et al. (2008) and Doubler et al. (2015), the criteria for identifying different meridional LLJs are as follows: for

147   southerly LLJs (S-LLJs), the jet-core wind direction is between 113° and 247°; for northerly LLJs (N-LLJs), the jet-

148   core direction is between 293° and 67°. These criteria are also used in this study.

149   Based on the identification criteria above, we determined if the LLJ existed at each grid point and consequently

150   counted the occurrences of S-LLJs and N-LLJs. We also calculated the frequencies of LLJs in different seasons or

151   time steps. The frequency is defined as the percentage of the total number of occurrences for the selected accumulation

152   period. We generated the frequency distribution maps for LLJs in North America, which are illustrated in Section 3.

153   **3.   The patterns of North American LLJs**

154   **3.1 Analysis of atmospheric circulation**

155   This study adopts model data to capture the climatological features of LLJs in North America. Considering the

156   relationship between LLJs and synoptical systems, we evaluated the ability of the convection-permitting model to

157   simulate the background atmospheric circulation. Figure 2 depicts the simulated multi-year analysis of geopotential

158   heights at 500 hPa and sea-level pressure isobars for summer and winter. In summer, at a height of 500 hPa (Figure

159   2a), In summer, the model depicts a trough in the east of the continental US, a ridge over the Rocky Mountains, and

160   the upper-air subtropical anticyclone crossing the southern US. At sea level (Figure 2b), the model captures the Azores

161   High-Pressure area in the Atlantic Ocean and the Hawaiian High-Pressure area in the Pacific.

162   In winter, the contours at the pressure value of 500 hPa (Figure 2c) show stronger fluctuating characteristics: the

163   eastern trough and western ridge over the continent strengthen, and the polar vortex extends to the northern US, while

164   most of North America is controlled by a cold high-pressure system. In addition, the subtropical anticyclone is too

165   weak to be found within the study domain. On the other hand, most of North America is controlled by a cold high-

166   pressure system at sea level (Figure 2d), and parts of the Icelandic Low and Aleutian Low appear on both east and

167   west of Canada, even though their centers are not captured in the domain. To summarize, the convection-permitting

168   model can simulate the features of semi-permanent centers of atmospheric circulations in North America, thus

169   demonstrating its strength in identifying the LLJs in this area.
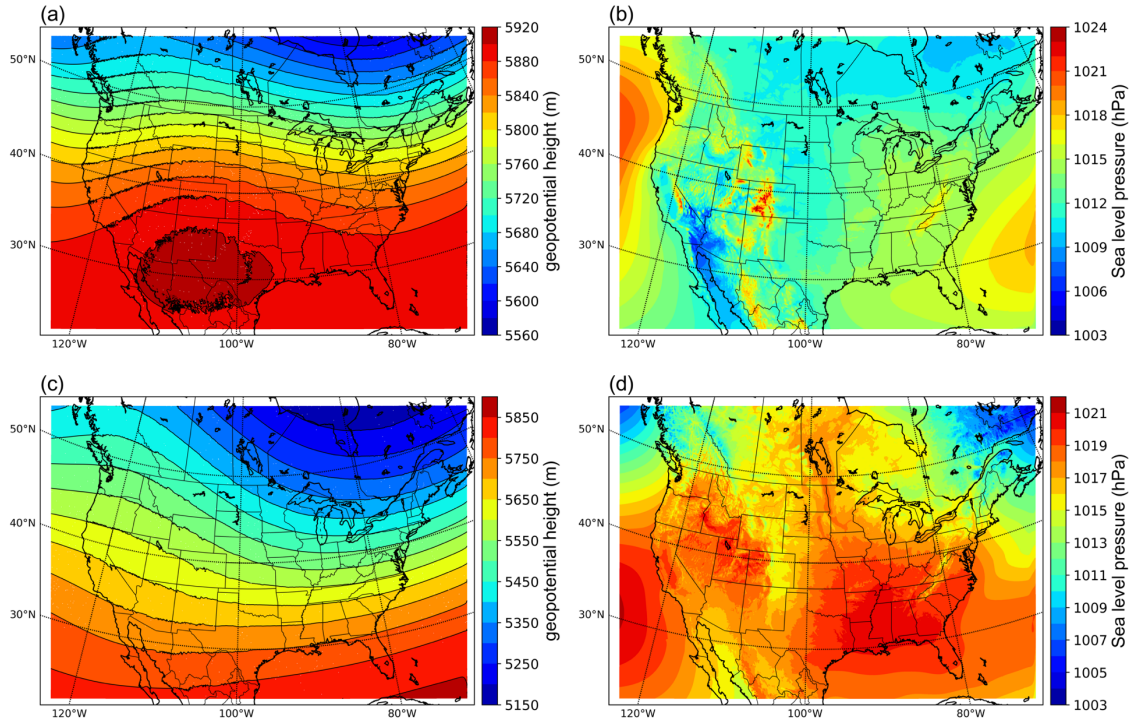
Figure 2. Multi-year patterns of atmospheric circulations simulated by the convection-permitting model: (a) summer 500 hPa geopotential height; (b) sea-level pressure in summer; (c)-(d) the same variables but in winter.

3.2 Seasonal variations of LLJs

3.2.1 Northerly LLJs

Figure 3 illustrates the seasonal frequency distribution of Northern Low-Level Jets (N-LLJs). The frequency is defined as the ratio of the total number of LLJ occurrences to the total number of time steps in each season. Notably, the California coastal LLJ peaks during the summer months (June, July, and August (JJA)), where frequencies exceed 25% over a broad area stretching from the southern Oregon coast to central California. In these regions, frequencies above 5% can even extend into the Pacific Ocean near northern Baja California. However, transitioning from summer to autumn (September, October, and November (SON)), there is a sharp decline in the frequency of this LLJ, dropping to only 5%-15% within the core region, predominantly along the northern California coast. In winter (December, January, and February (DJF)), occurrences are sparse, at approximately 1%-2%.

Conversely, various N-LLJ phenomena are more prevalent during the colder seasons. These jets primarily occur near the eastern slopes of significant terrains such as the Rocky Mountains, Appalachian Mountains, and the Quebec

186 Labrador Plateau. High frequencies (>10%) are observed from western Alberta to Oklahoma during winter, with hot

187 spots sporadically located in Alberta, Montana, Wyoming, and Colorado, where frequencies reach about 20%,

188 particularly between Colorado and Wyoming. In more than 25% of the wind profiles analyzed, N-LLJs were

189 identifiable. Along the Eastern US coast, N-LLJs predominantly stretch from Maine to South Carolina with peak

190 frequencies of approximately 15%-20%. In eastern Quebec, N-LLJs are most frequent in winter, exceeding 25%. The

191 simulation also detects the presence of N-LLJ in about 10% of the time steps over Hudson Bay. Notably, the

192 frequencies of all aforementioned N-LLJs significantly diminish in spring, becoming scarcely detectable in summer

193 with frequencies mostly under 5%.
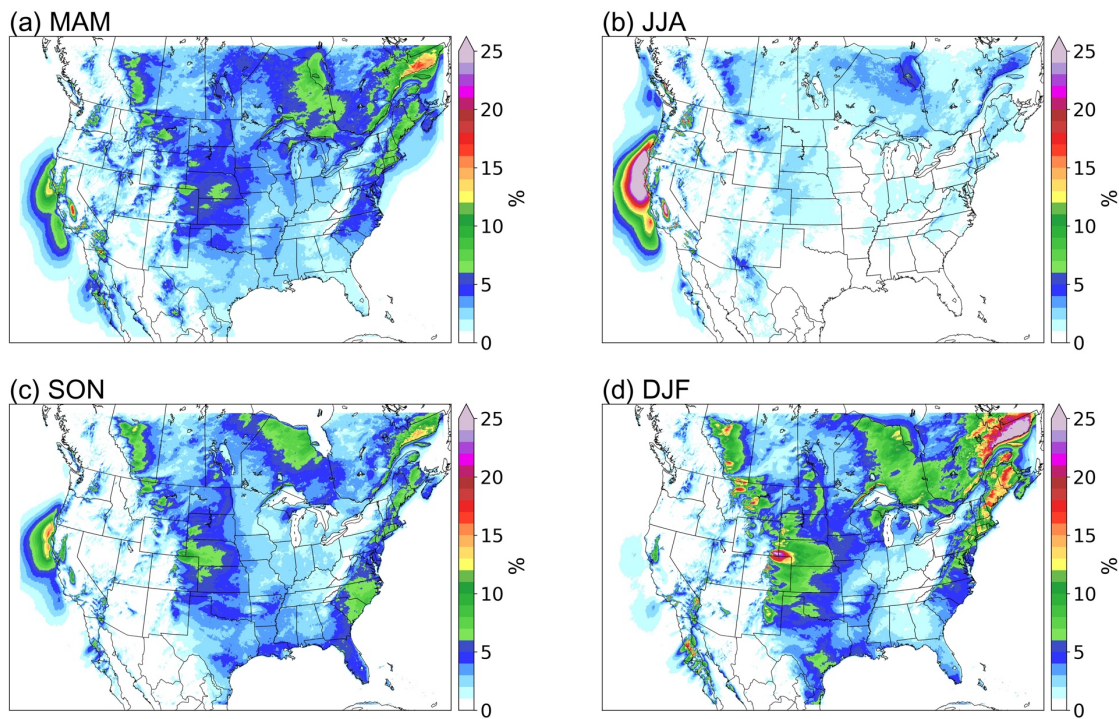
195 **Figure 3. Seasonal occurrence frequency of N-LLJs. Frequency shown here is calculated by counting the number of**
196 **occurrences of LLJs in each three-hourly time step and then dividing the total number of LLJs in each season by the number**
197 **of time steps in that season.**

198 **3.2.2 Southerly LLJs**

199 As to the patterns of S-LLJs in different seasons (see Figure 4), during winter, frequencies exceeding 10% are observed

200 across a vast area spanning from south Texas and the western Gulf of Mexico to southern Iowa, depicted as a deep

201 green area in Figure 4d. The greatest frequencies of S-LLJs (>20%) are found along the border between northeastern

202   Mexico and the United States. In addition, about 15% of the simulated wind profiles in south-central Texas are

203   identified as S-LLJs (red clusters). In the spring (March, April, and May), the frequency expands significantly in >10%

204   of areas, with clear S-LLJ distributions detected in Manitoba, Saskatchewan, and other parts of Canada. The highest

205   frequencies are still found in the Texas-Mexico area, where the magnitude of these frequencies increases to over 25%.

206   This region (colored purple) also extends northward to occupy most of Texas. In winter, S-LLJs with occurrence

207   frequencies of above 15% extend to near Colorado and Nebraska.

208   By summer, the area with frequencies greater than 10% no longer reaches to the central Canadian prairie provinces.

209   The S-LLJs over the western Gulf of Mexico become nearly indiscernible in modeled data, with frequencies

210   approaching 0%. Conversely, the area with frequencies exceeding 25% expands northward and is segmented into three

211   distinct parts: along the northeast Mexico-Texas border, west-central Texas, and the central US Great Plains (western

212   Oklahoma and southern Kansas). Regions where over 15% of wind profiles are identified as S-LLJs also spread from

213   Colorado to near South Dakota.

214   In the fall, the magnitude of the frequency of S-LLJs decreases dramatically in the central US Plains and Texas. The

215   frequency still maintains a level greater than 15% in most areas, but with a maximum frequency of only 20% and

216   sporadically located in southwest Texas. The frequencies greater than 10% again expand northward and eastward in

217   this season, reaching Manitoba and Ontario.

218   Additionally, several smaller-scale S-LLJs are evident on the seasonal S-LLJ distribution map. In spring, a narrow

219   region of S-LLJs with a frequency greater than 5% along the eastern side of the Appalachians extends from Georgia

220   through the western Atlantic to southern Nova Scotia. Near eastern Maryland over the Atlantic, the frequency of S-

221   LLJs can exceed 10%. This narrow frequency belt persists through summer with the same coverage, though the

222   frequency magnitude diminishes, and the presence of frequencies greater than 10% is no longer visible. In winter, a

223   region where S-LLJ frequency exceeds 5% stretches from southwest Oregon to the west coast of British Columbia,

224   Canada. However, by spring, S-LLJs with frequencies above 5% occur solely over the ocean west of British Columbia,

225   and in summer, S-LLJs are virtually undetectable in this region.
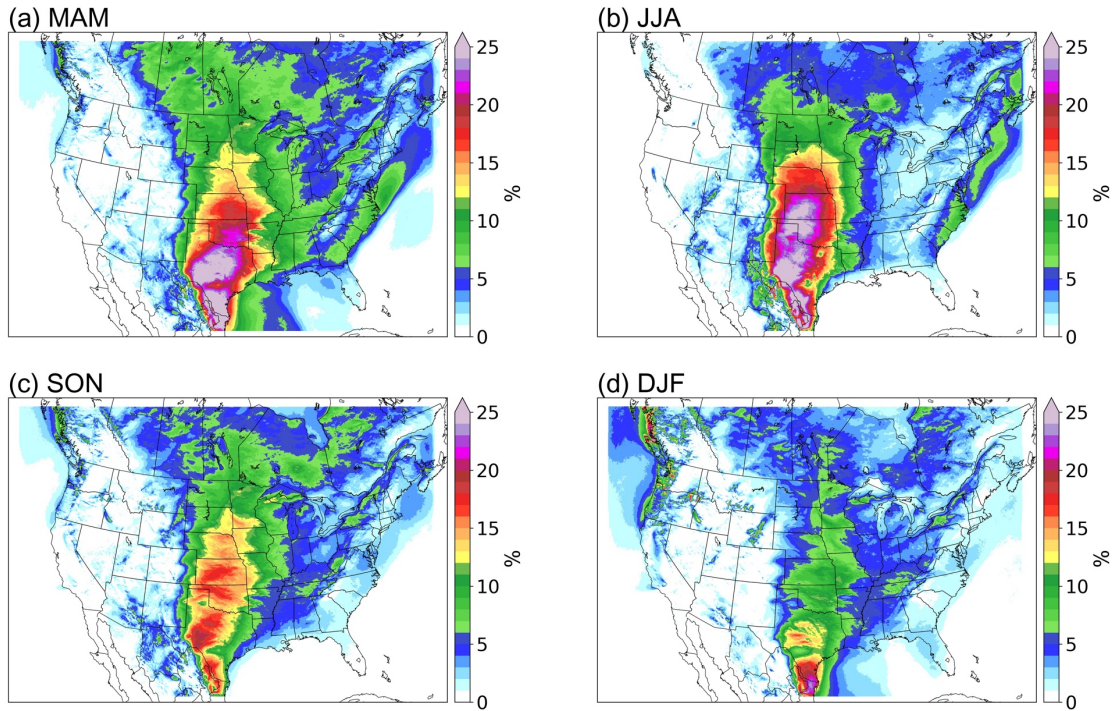
227 **Figure 4. Seasonal frequency of S-LLJs.**

228   To summarize, for the LLJ systems that have been investigated by many researchers, the convection-permitting WRF

229 model performs well in observing the Great Plains S-LLJ and California coastal N-LLJ during the summer. But as to

230 the winter LLJs that lack attention, it is essential to compare and validate the occurrence and features revealed by

231 WRF simulation. Therefore, the ERA5 reanalysis dataset is applied in this study for capturing the LLJs in winter using

232 the same criterion. Appendix after the text shows the results of the comparison between ERA5 and WRF simulation.

233 **3.3 Diurnal variations of LLJs**

234 To show the diurnal features of the LLJs, we selected summer and winter as the representative seasons because S-

235 LLJs and N-LLJs occur most frequently in these seasons, respectively. Below, the descriptions are divided into N-

236 LLJs and S-LLJs.

237 **3.3.1 Northerly LLJs**

238 The California coastal N-LLJ is the most highlighted low-level jet system in this region in summer. As seen in Figure

239 5, it occurs throughout the day over the eastern Pacific Ocean from Oregon to the California coast. Figure 5 also shows

240 that the California Coastal N-LLJ has diurnal characteristics: from 21 UTC (1 pm LST in California), the low-level

jet begins to develop, with a N-LLJ frequency of >30%, expanding until it reaches its maximum at 03 UTC – 06 UTC. Then the high-frequency coverage of the California coastal LLJ gradually shrinks, reaching the minimum at 18 UTC and only existing off the northwest coast of California.
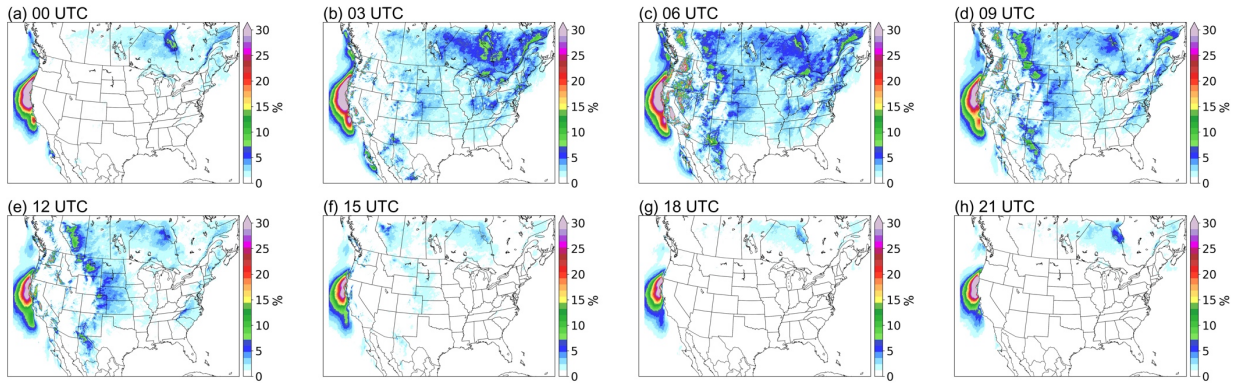
Figure 5. Diurnal frequency of N-LLJs in the summer (JJA).

In winter (Figure 6), three types of N-LLJs over the Hudson Bay Lowlands, the eastern slopes of the Quebec Labrador Plateau, and the Appalachians display similar diurnal fluctuations. All three N-LLJs reach their highest frequency at 03 UTC (10 pm EST) and their lowest at 18 UTC (1 pm EST). The only difference among the three types is that the smallest frequency of the Quebec N-LLJ still endures at a level of greater than 15%, while the other two N-LLJs mostly have frequencies of about 5%. The smallest frequency (~5%) of N-LLJs occurs downstream of the Rocky Mountains (over Alberta, Montana, and Kansas) at 21 UTC. In the subsequent development stage, the changes in the sporadic hot spots distributed near the eastern boundary of the Rocky Mountains are more significant. As seen in Figure 6, frequency starts growing from 00 UTC and then peaks at 12 UTC, especially the wind maxima located in Colorado, Wyoming, and Kansas, where the highest frequency can be >25%.
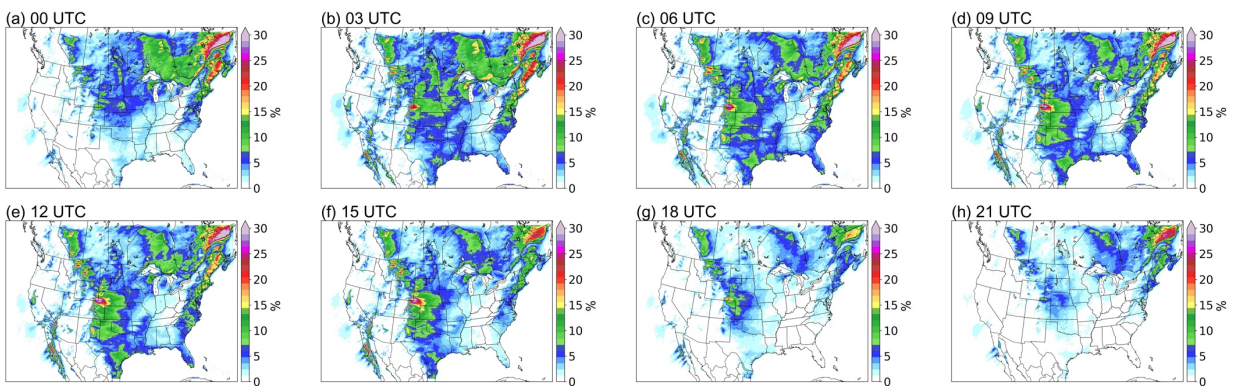
256 **Figure 6. Diurnal frequency of N-LLJs in winter (DJF).**

257 **3.3.2 Southerly LLJs**

258 In summer, the Great Plains S-LLJ occurs more frequently than in other seasons, and its diurnal variability is also the

259 strongest in this season (see Figure 7). At noon local time and in the afternoon (18 UTC – 00 UTC, 12-18 CST), almost

260 no S-LLJs occur over the central US (frequency <5% or about 0%). In contrast, the Great Plains LLJ begins to develop

261 at 03 UTC, when a frequency of over 25% extends from Mexico to Kansas. It reaches maximum strength at midnight

262 (06 UTC – 09 UTC, 00 – 03 CST), when the frequency reaches over 30% and the high-frequency coverage enlarges

263 to the Dakotas, the border of the eastern Rocky Mountains, and western Minnesota, Missouri, and Louisiana. Summer

264 S-LLJs are also active in southern Canada at night and in the early morning. In Saskatchewan, Manitoba, and central

265 Ontario (03 UTC – 12 UTC, as shown in Figure 7), S-LLJs are found with frequency >15%. In the eastern US and

266 Atlantic, S-LLJs occur most frequently at midnight (03 UTC – 06 UTC).
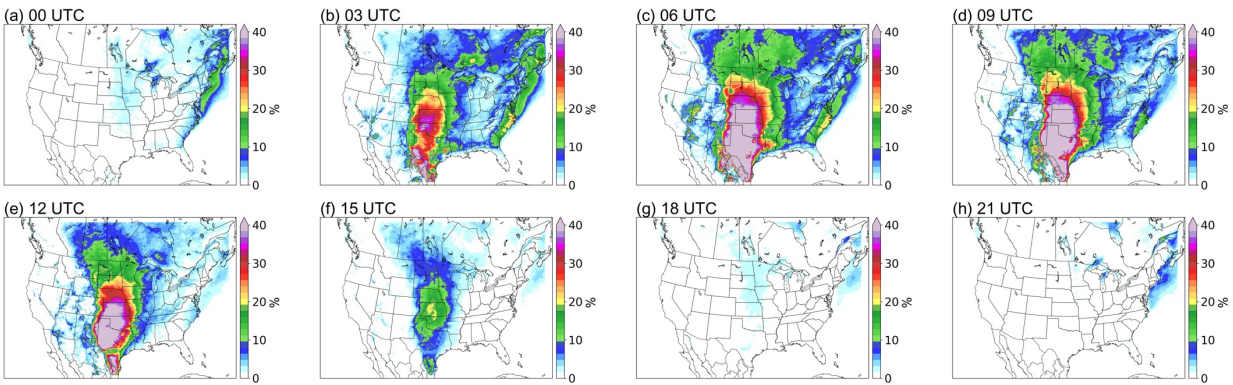
267

268 **Figure 7. Diurnal frequency of S-LLJs in summer (JJA).**

269 For the cold season (Figure 8), even though the Great Plains LLJ is the most inactive based on the description in

270 section 3.2, it still has a clear diurnal variation. Compared with the results in summer, the diurnal cycle of Great Plains

271 LLJ in winter is not that pronounced: It mainly occurs over the western Gulf of Mexico and southern Texas, with the

272 frequency in the afternoon (18 UTC – 21 UTC) declining to 5-10%. The S-LLJ develops from 03 UTC, gradually

273 generating two high-frequency (20%-25%) centers in mid- and southeastern Texas at 06 UTC – 12 UTC. As for the

274 S-LLJ near Vancouver Island, it is hard to see the diurnal variability: There is only a slight magnitude growth of

275 frequency from the afternoon (00 UTC) to the evening (06 UTC), and the coverage is almost the same.
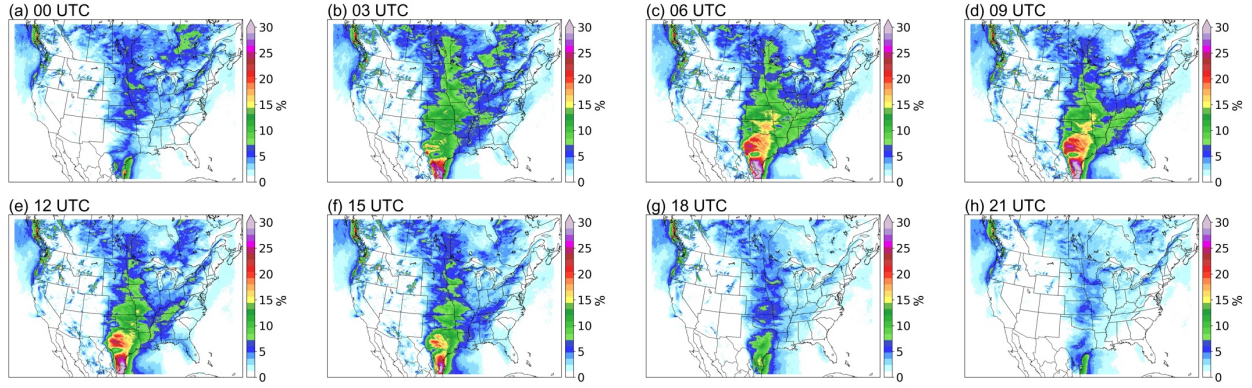
Figure 8. Diurnal frequency of S-LLJs in winter (DJF).

4   Formation and evolution mechanisms of various LLJs

Section 3's results illustrate the occurrence frequency of LLJs over North America, particularly their seasonal and

diurnal features. To explain the mechanisms, the inertial oscillation theory from Blackadar (1957) is used. Using this

theory, we start from the horizontal momentum equations and divide the actual horizontal wind u/v into two

components—geostrophic wind u_g/v_g and ageostrophic wind u_a/v_a:

$$\frac{d(u_g + u_a)}{dt} = -\frac{1}{\rho}\frac{\partial P}{\partial x} + f(v_g + v_a) \tag{1.1}$$

$$\frac{d(v_g + v_a)}{dt} = -\frac{1}{\rho}\frac{\partial P}{\partial y} - f(u_g + u_a) \tag{1.2}$$

In which ρ is air density, P is pressure, and f is the Coriolis parameter. Assuming the horizontal pressure gradient is

fixed, the geostrophic wind is a constant as well, which means $\frac{du_g}{dt} = \frac{dv_g}{dt} = 0$:

$$\frac{du_a}{dt} = -\frac{1}{\rho}\frac{\partial P}{\partial x} + f(v_g + v_a) \tag{2.2}$$

$$\frac{dv_a}{dt} = -\frac{1}{\rho}\frac{\partial P}{\partial y} - f(u_g + u_a) \tag{2.2}$$

When the definition of geostrophic wind $u_g = -\frac{1}{\rho f}\frac{\partial P}{\partial y}$ and $v_g = \frac{1}{\rho f}\frac{\partial P}{\partial x}$ is combined, the equation (2) is:

$$\frac{du_a}{dt} = fv_a \tag{3.1}$$

$$\frac{dv_a}{dt} = -fu_a \tag{3.2}$$

295

296   If $\frac{d}{dt}$ is taken to both sides of the equations (3), then we get $\frac{d^2 u_a}{dt^2} = -f^2 u_a$, and $\frac{d^2 v_a}{dt^2} = -f^2 v_a$, thereby:

$$u_a = c_1 \cos(ft) + c_2 \sin(ft) \qquad (4.1)$$
$$v_a = c_2 \cos(ft) - c_1 \sin(ft) \qquad (4.2)$$

300   Therefore, according to the equations (4), the ageostrophic wind should theoretically have a circle-pattern variation

301   and the vector must rotate clockwise with a period of $2\pi/f$ (Blackadar, 1957; Van de Wiel et al., 2010). Under the

302   condition of a constant geostrophic wind—when the ageostrophic vector rotates from the opposite to the same

303   direction of geostrophic wind—the wind transitions from subgeostrophic to supergeostrophic. This change occurs

304   because of decoupling with surface friction effects, then the wind gets unbalanced.

305   Other theories also help explain the formation of LLJs, such as the sloping-terrain thermodynamic mechanism (Holton,

306   1967) and background synoptic system forcing (Uccellini et al., 1987). To understand the characteristics of the LLJs

307   in this study, three typical cases are analyzed: Great Plains S-LLJ, Quebec N-LLJ, and California coastal N-LLJ. The

308   locations for extracting data are shown in Figure 1 (solid lines and stars a, b, c).

4.1 Great Plains S-LLJ

310   As Section 3's results show (see Fig. 7), the Great Plains S-LLJ typically occurs in summer and more frequently at

311   night. To investigate its associated meteorological condition, this study extracts all the Great Plains S-LLJ cases occurs

312   at the jet core in JJA. The jet core is defined by where the mean meridional wind is the strongest on the cross-section,

313   and it locates at star A (shown in figure 1). The mean sea-level pressure and 800 hPa geopotential height are shown

314   in Figure 9a and 9b, respectively. The background large-scale circulations indicate that, at all the time points when

315   the Great Plains S-LLJ occurs, the range of the subtropical anticyclone extends east of the Great Plains at both ground

316   and low-level atmosphere. A high-pressure ridge is located near the gulf coast of Mexico and Texas (Figure 9b). Thus,

317   clearly, the zonal pressure/geopotential gradient in the central US guides the dominant southerly winds around this

318   region. The cross-section in Figure 9c illustrates a strong baroclinicity and shows that the isentropic line incline moves

319   from east to west, as is typical for the sloping-terrain heating effect (Holton, 1967). This effect generates an upslope

320   wind on the east side of the slope, and the airstream gradually turns northward due to the Coriolis force, creating the

321   southerly LLJs. On the other hand, as can be seen in the frequency cycle in Figure 9d, at noon local time (at the

 selected point-a in Figure 1), the frequency of the Great Plains LLJ is very low (close to 0%), rising to more than 40%

323 after 18 LST even if the radiation is not at the day's peak.

324
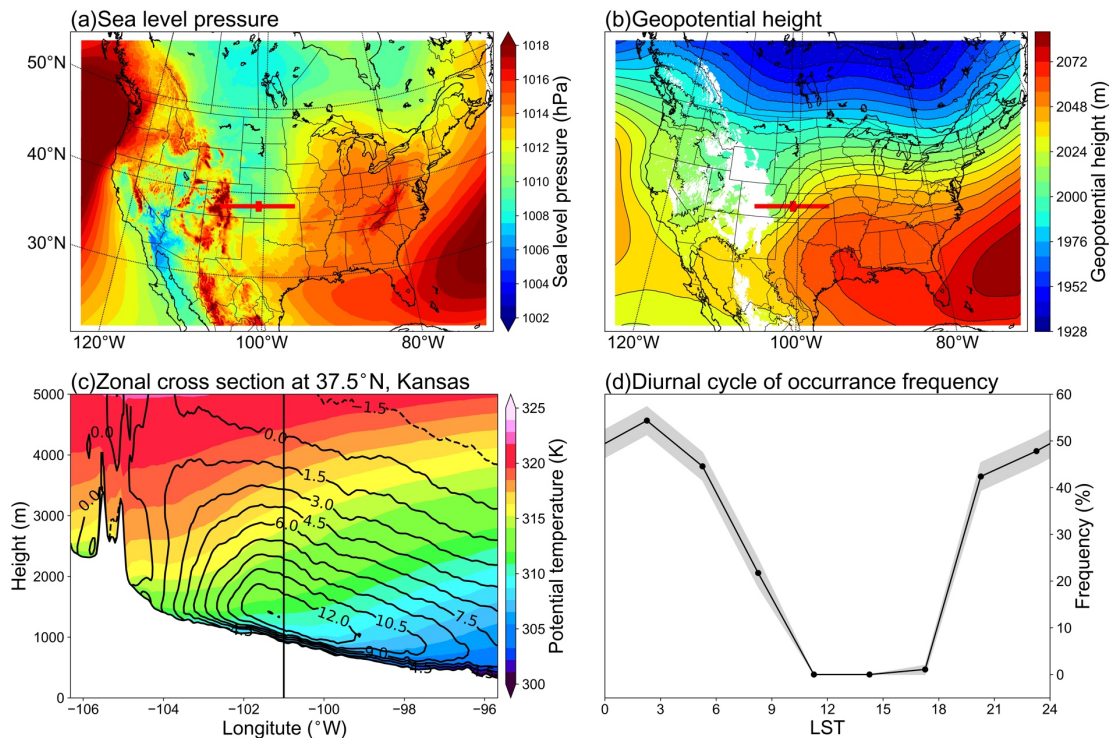
Figure 9. Background circulations of the Great Plains S-LLJ in JJA: (a) sea-level pressure, (b) geopotential height of 800 hPa, (c) cross section including meridional winds (lines) and potential temperature (shading), and (d) diurnal cycle of frequency, with the shaded 95% confidence intervals. The red lines and points in (a) and (b) show the position of cross-section and chosen jet core, the vertical line in (c) shows the zonal location of the chosen jet core.

329 To explain the nighttime enhancement of S-LLJ, we analyzed the wind vectors using inertial oscillation theory. To

330 show more significant diurnal variation, all the time points, including the LLJs that did not occur, were considered.

331 Figure 10a is the hodograph of jet-core winds at point-a near the Great Plains, and their temporal mean is computed

332 at 3-hourly intervals in summer. It is noted here that the "jet-core" means the position where LLJ occurs horizontally

333 the most frequently on the cross-section. Compared with the mean actual wind (blue arrow), the deviation at each

334 local time shows a clear clockwise rotation. The wind speed begins increasing after 17 LST. Nevertheless, the analysis

335 for Figure 9 indicates the sloping heating effect, meaning that the geostrophic wind is not fixed.

336 Thus, to obtain the ageostrophic winds, we computed the geostrophic components by pressure gradient and subtracted

337 them from the actual airflow. According to the aforementioned definition of geostrophic wind, u_g and v_g are

338   calculated by the horizontal pressure gradient $\frac{\partial P}{\partial y}$ and $\frac{\partial P}{\partial x}$, respectively. By choosing four grids surrounding point-a, we

339   first interpolated the pressure value to the same level as the LLJ core height. Then, we adopted the central difference

340   equation $\frac{\Delta P}{\Delta x} = \frac{P_{i+1} - P_{i-1}}{x_{i+1} - x_{i-1}}$ or $\frac{\Delta P}{\Delta y} = \frac{P_{i+1} - P_{i-1}}{y_{i+1} - y_{i-1}}$ to obtain the pressure gradients at point-a, where i is the index of the grid

341   point at point-a.

342   Figures 10b and 10c display geostrophic wind vectors (blue arrows) and ageostrophic vectors (pink) at noon and

343   midnight. The southerly geostrophic flows are much stronger in the afternoon (10b) than at midnight. The ageostrophic

344   winds flow mostly in the opposite direction, limiting the actual wind speed. At night (10c), the geostrophic wind

345   direction rotates clockwise from that of the afternoon as the pressure gradient changes. Considering the relative

346   positions of blue and pink vectors at 23 LST and 01 LST, ageostrophic flow has rotated roughly 150 degrees to

347   enhance the geostrophic winds, thereby creating a super-geostrophic state. Although the inertial oscillation theory can

348   help explain some aspects of wind behavior, the real situation is more complex than initially thought. Figures 10b and

349   10c indicate that by 02 LST, the wind is almost entirely geostrophic with only negligible ageostrophic perturbations.

350   This suggests that the diurnal changes in the geostrophic wind and pressure gradient may provide a complicating

351   background that prevents the inertial oscillation theory from fully prevailing. While the inertial oscillation theory can

352   provide valuable insights, it should not be relied upon as the sole explanation for LLJs at the Great Plains. Instead, a

353   more comprehensive understanding of atmospheric dynamics is necessary to fully comprehend the behavior of the

354   wind, particularly when dealing with diurnally changing conditions. Figure 10d compares different meridional wind

355   components' amplitudes. The geostrophic wind contributes significantly to the southerly wind during the day, peaking

356   at 14 LST (blue bars). The northerly ageostrophic wind (red bars) is highest during the day, indicating the strongest

357   negative impact from friction. The meridional ageostrophic component decreases and eventually reverses at 23 LST,

358   showing a process from sub- to super-geostrophic status. In summary, the thermodynamic circulation near the slopes

359   of the Great Plains contributes to the strong southerly airflow, while the inertial oscillation plays a critical role in

360   forming the nocturnal southerly LLJ.
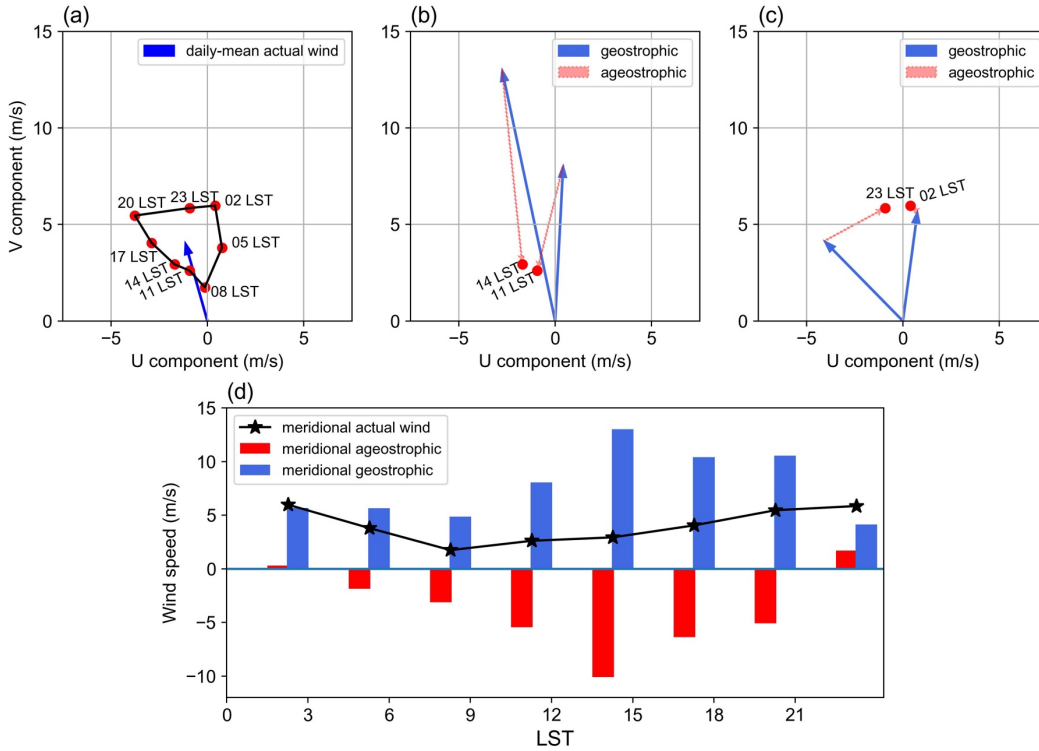
Figure 10. (a) Hodograph of jet-core winds for the Great Plains S-LLJ every 3 hours over the whole JJA (red dots – solid line) and the daily averaged actual wind velocity (blue vector); vectors of mean jet-core geostrophic winds (solid blue) and ageostrophic winds (dashed red) at (b) 11/14 LST and (c) 23/02 LST; (d) diurnal cycles of meridional components of actual (black line), geostrophic (blue bars), and ageostrophic winds (red bars).

4.2 Quebec N-LLJ

Similarly, for the Quebec N-LLJ that is typically observed in winter, we selected all the LLJ cases at point-b (see the position in Figure 1) in DJF to generate the background circulation pattern. The background large-scale circulations indicate that the northeastern coast of Canada lies to the west of a strong surface low-pressure system (Figure 11a), while in the lower troposphere, a ridge on the east side of Hudson Bay occupies the Labrador Plateau (Figure 11b). This combination brings the northerly momentum to the downstream eastern coast. In fact, the background circulation is consistent with the shallow baroclinic structure of Quebec N-LLJ in winter, that is, the thermal difference between relatively warm sea and cold land. The cross-section in Figure 11c shows the thermodynamic structure of this N-LLJ: A well-defined low-level jet core is located above land and close to the coastline (approximately 63°W). With a maximum wind speed of more than 16 m s-1 and a height of about 400 m, the jet core is located above the mixed layer

377 under the warm air covering and on the land side. Notably, the steep isentropic lines slope towards the ocean and

378 finally sink at the position of 60°W. The onshore isentropic lines are flat and dense above the LLJ core, which means

379 the environment is quite stable. This is helpful to maintain the structure of the LLJ, when vertical motion is inhibited,

380 and horizontal wind is enhanced. Compared with the sloped isentropic lines in the Great Plain S-LLJ case (Figure 9c),

381 the stability over Great Plain is not as high as in this case, so this difference in stability helps explain the variation in

382 wind speeds between these two cases.

383 In addition, the diurnal cycle of frequency (Figure 11d) shows that the diurnal signal and peak frequency of Quebec

384 N-LLJ are much weaker than the Great Plains S-LLJ, becoming weakest at noon and peaking at midnight, which is

385 consistent with the results reported in Section 3. This diurnal variation can be explained by the baroclinicity near this

386 region: At night in winter, the land temperature drops faster than the ocean temperature due to radiative cooling,

387 enhancing the land-sea contrast and thereby the thermal wind above. The gentle slope on the east of the Labrador

388 Plateau could generate the slope heating effect in the daytime. In this way, the related temperature gradient from east

389 to west offsets the land-sea thermal difference.
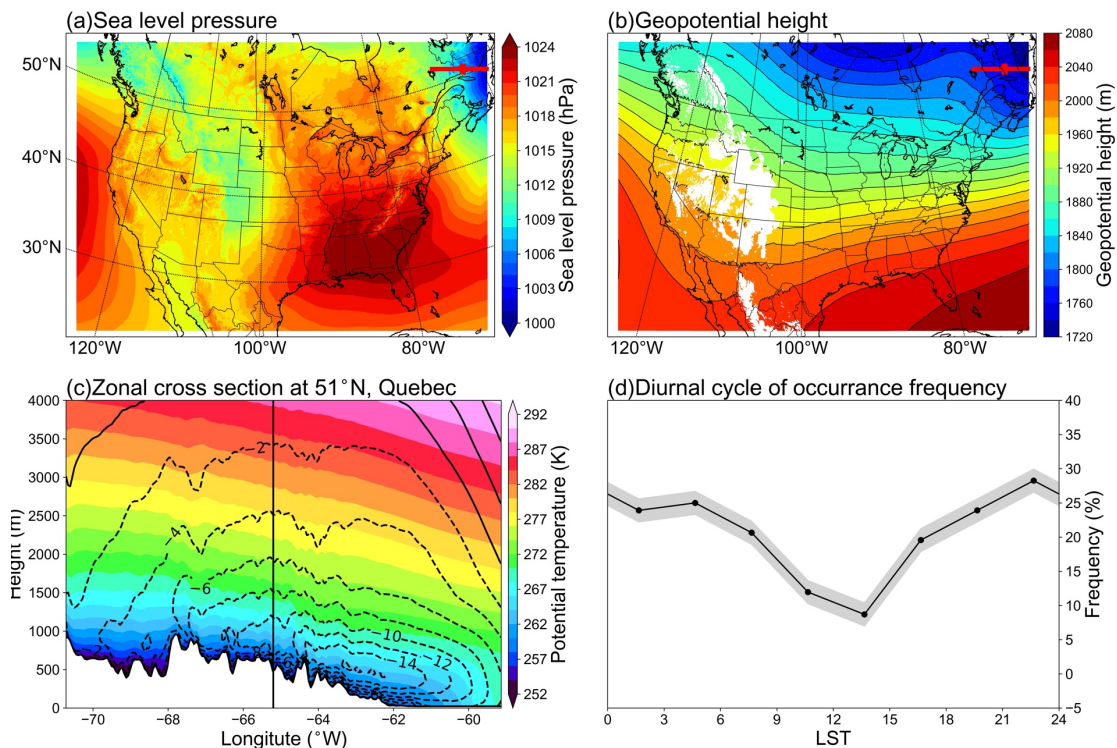
390

391 **Figure 11. Background circulations of the Quebec N-LLJ in DJF: (a) sea-level pressure, (b) geopotential height of 800 hPa,**

392 **(c) cross section including meridional winds (lines) and potential temperature (shading), and (d) diurnal cycle of frequency**

with the shaded 95% confidence intervals. The red lines and points in (a) and (b) show the position of cross-section and

chosen jet core, the vertical line in (c) shows the zonal location of the chose jet core.

As for the impact of inertial oscillation on the Quebec N-LLJ, the hodograph of averaged 3-hourly winds extracted at point-b (Figure 12a) also illustrates a clear clockwise rotation of wind deviations compared with the daily mean (blue arrow). Figure 12b and 12c show that the geostrophic and ageostrophic wind vectors contribute to the diurnal cycle in the afternoon and morning, respectively. Even though the direction of geostrophic wind changes significantly, the relative angles between ageostrophic and geostrophic arrows indicate that the ageostrophic flow rotates clockwise. The geostrophic wind is weakened by ageostrophic wind in the afternoon (Figure 12b), whereas the supergeostrophic state is generated in the morning (Figure 12c).

Focusing only on the meridional amplitudes validates this characteristic. In Figure 12d, the blue line that represents the mean actual meridional wind has the same diurnal trend as the frequency variation in Figure 11d. The northerly wind is weakest in the afternoon, peaking at night and in the early morning. Similarly, the variation of meridional geostrophic flow has a consistent phase with the actual meridional wind, which is explained by the baroclinic structure near the Quebec coast mentioned above. The meridional ageostrophic wind in this region also promotes the formation of N-LLJ. The ageostrophic wind drags the geostrophic component in the afternoon, before reversing to a consistent direction with the northerly geostrophic flow at night and in the morning. This trend is also the result of decreasing friction after sunset. Therefore, the evolution of Quebec N-LLJ derives from both inertial oscillation and land-sea thermal contrast in winter.

411
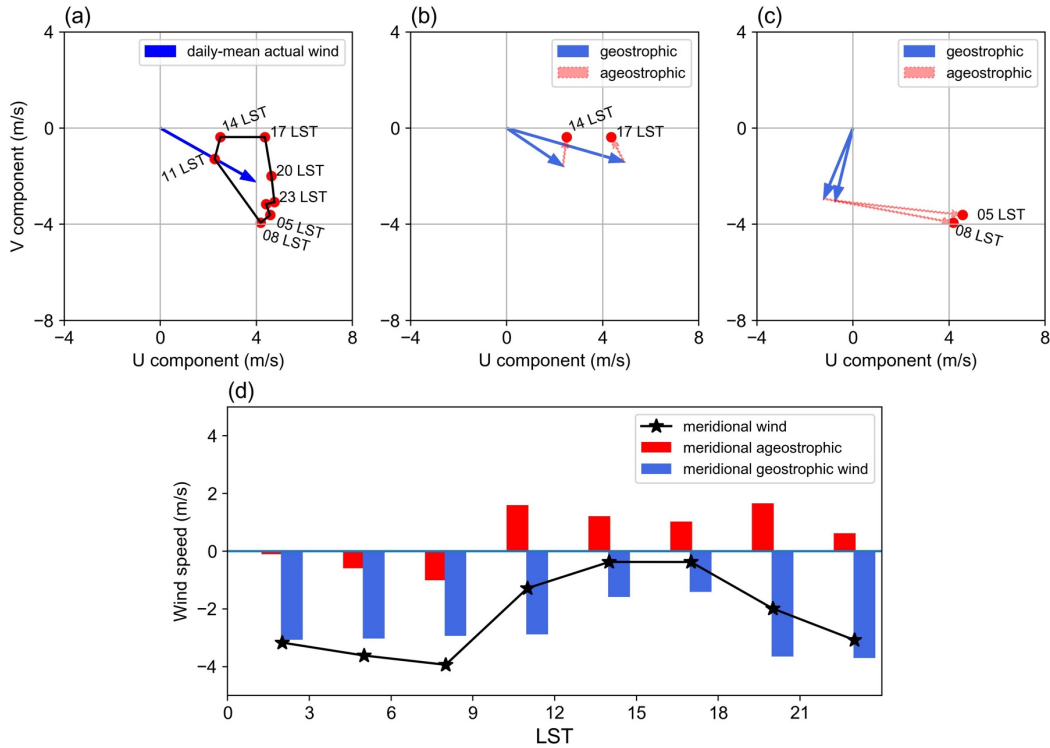
Figure 12. (a) Hodograph of jet-core winds for the Quebec N-LLJ every 3 hours over the whole DJF (red dots – solid line)
and the daily averaged actual wind velocity (blue vector); vectors of mean jet-core geostrophic winds (solid blue) and
ageostrophic winds (dashed red) at (b) 14/17 LST and (c) 05/08 LST; (d) diurnal cycles of meridional components of actual
(black line), geostrophic (blue bars), and ageostrophic winds (red bars).

4.3 California coastal N-LLJ

The California coastal N-LLJ is similar to the one in Quebec, but it occurs more often in summer afternoons or

evenings over the ocean. Figure 13a shows that a relatively strong high-pressure system is located on the east coast of

the Pacific Ocean, trending NE-SW, although half of the structure is beyond the boundary of the domain. On the 800

hPa isobaric surface in Figure 13b, there is also an anticyclone system in the same location, whose eastern contour is

roughly parallel to the coastline, guiding the airflow to the south. Therefore, this pair is also forced by the thermal

difference between land and sea, but contrary to the LLJ in Quebec, in summer, when the California LLJ occurs

frequently, it has the characteristics of the cool sea-hot land. Figure 13b also shows that the isobars near Cape

Mendocino are relatively strong, making the ridge of high pressure extend northeastward of the Cape. This extension

is generally believed to occur due to pressure perturbation caused when northerly winds converge at this position after

427 being obstructed (Rahn and Parish, 2007). Regarding the cross-section structure shown in Figure 13c, the jet core is

428 located at steep isentropic lines above the ocean at a height of 500 m. On the coast of California, the LLJ is close to

429 the mountains. The maximum central wind speed of California coastal LLJ exceeds 20 m s-1, whereas Quebec N-

430 LLJ's max core wind is only about 14 m s-1. Based on baroclinicity, the isentropic lines slope towards the continent

431 and finally sink near the coastline.

432 The core wind speed in California's coastal LLJ is higher than that of Quebec's LLJ because the land-sea contrast is

433 more significant in summer than in winter and the formed sea breeze front generates flow convergence under the

434 blockage caused by the west coast mountains. On the other hand, the atmosphere over the sea is more stable because

435 the isentropic lines are flatter and denser than Quebec's case, which also favors the development of LLJ. In contrast,

436 the east coast of Quebec is relatively gentle, which may account for its lower wind speed. California's LLJ occurs

437 frequently at each time step, and its diurnal signal is weaker compared, for example, to the signal in the Great Plain

438 S-LLJ. As well, the California signal stays at frequency of over 35%. California's LLJ occurs most frequently at

439 around 18 LST and starts to decline after sunset, which is generally consistent with the coastal baroclinicity.
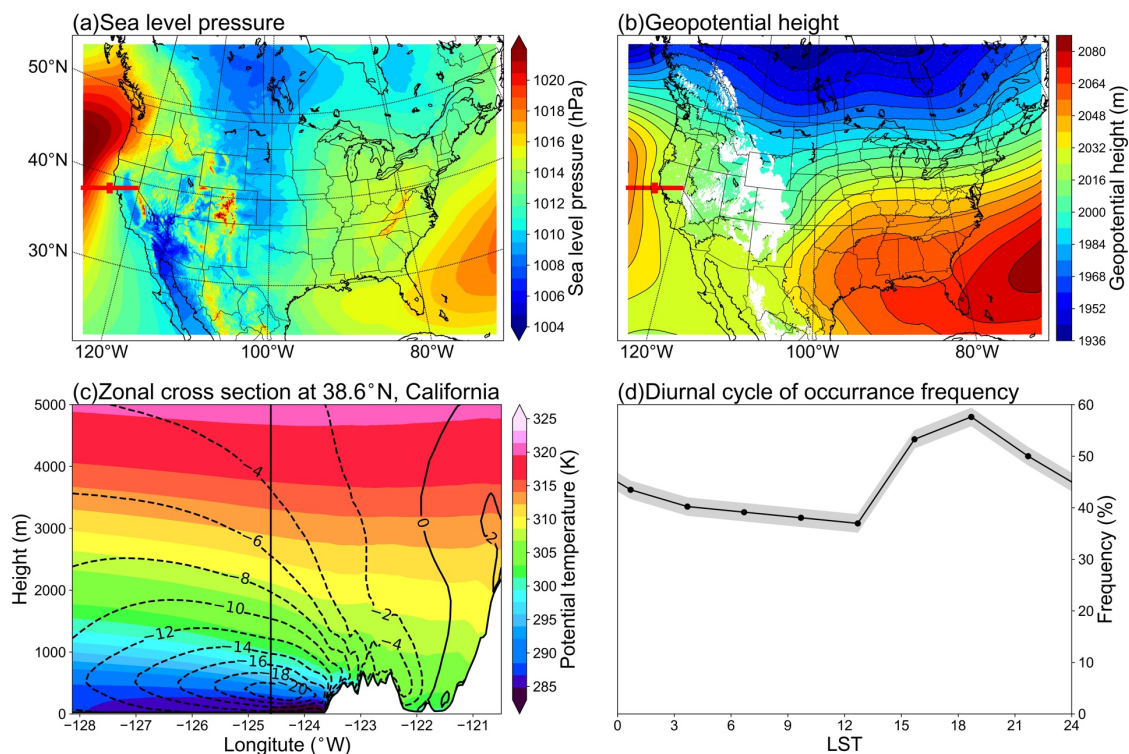
440

441 **Figure 13. Background circulations of the California coastal N-LLJ in JJA: (a) sea-level pressure, (b) geopotential height**

442 **of 800 hPa, (c) cross section including meridional winds (lines) and potential temperature (shading), and (d) diurnal cycle**

445

446 The wind deviations for California's N-LLJ shown in the hodograph (Figure 14a) still have a clockwise rotation in 24

447 hours. However, compared with the magnitude of the daily mean jet-core wind, this diurnal cycle is not quite as

448 obvious as the cycle for Quebec and Great Plain LLJs, but it is similar to the frequency cycle shown in Figure 13d. In

449 comparison between geostrophic and ageostrophic winds (Figure.14b and 14c), during the afternoon (15 and 18 LST),

450 the amplitude of geostrophic wind is the largest, and the ageostrophic flow diminishes the geostrophic wind. However,

451 in the morning 12 hours later, the relative angle between ageotrophic and geostrophic vectors does not change,

452 meaning that the ageostrophic wind is still weakening the geostrophic wind and that there is no rotation of the

453 ageostrophic wind, as Blackadar inertial oscillation theory describes. Figure 14d helps to explain the change in

454 meridional winds. Looking at the magnitudes of ageostrophic winds, one can see that all are weak and southerly and

455 that they do not exhibit a significant diurnal signal. Furthermore, the change of geostrophic wind is highly consistent

456 with the trend of the actual meridional wind. Thus, the N-LLJ in California can be considered mostly as geostrophic

457 and the diurnal variation as being related to the change in geostrophic winds.

458
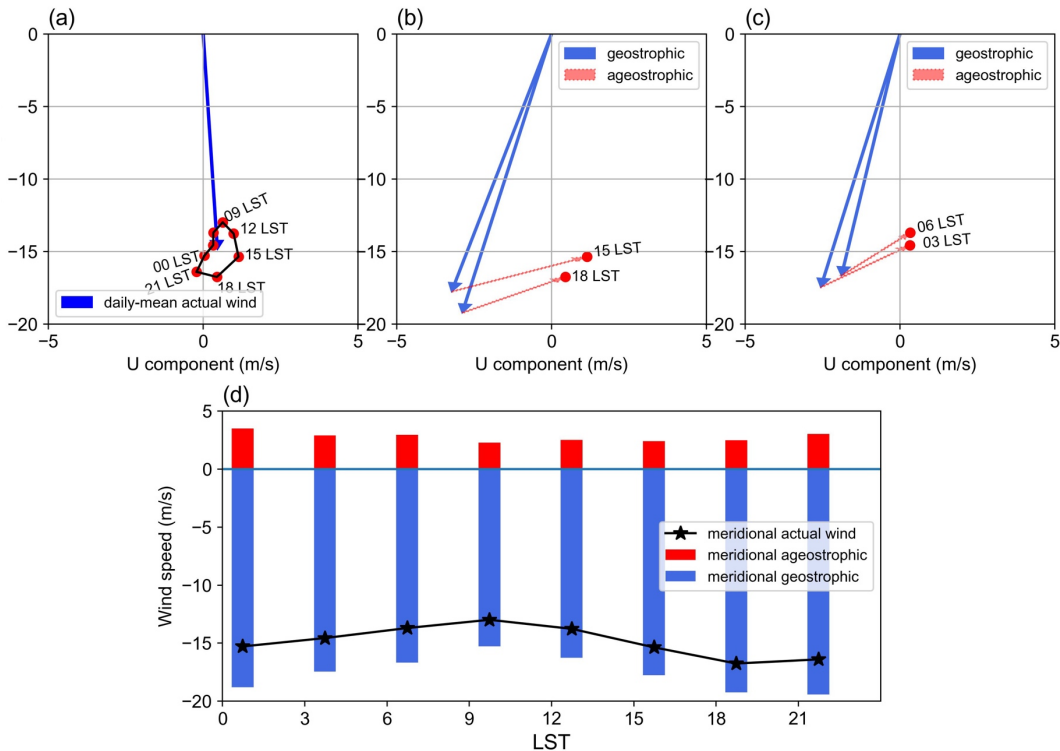
Figure 14. (a) Hodograph of jet-core winds for the California coastal N-LLJ every 3 hours over the whole JJA (red dots – solid line) and the daily averaged actual wind velocity (blue vector); vectors of mean jet-core geostrophic winds (solid blue) and ageostrophic winds (dashed red) at (b) 15/18 LST and (c) 03/06 LST; (d) diurnal cycles of meridional components of actual (black line), geostrophic (blue bars), and ageostrophic winds (red bars).

5   Discussion and conclusion

This study applied a convection-permitting WRF model to conduct the analysis of LLJs in North America. The previous research for LLJs mainly focused on observation data, which have no fine coverage in temporal or spatial resolution. The studies using in-situ observations may ignore some important features. Despite their better coverage, reanalysis datasets usually have a coarse spatial resolution, and can introduce large inaccuracies in the identification of LLJs. In addition, the application of general numerical modeling cannot avoid the uncertainty caused by parameterizing small-scale physical processes. In contrast, high-resolution convection-permitting climate simulations can provide relatively more comprehensive descriptions of LLJs, especially for areas with complex geographic conditions or regions that lack soundings. Previous studies using high-resolution models conducted case analyses only of LLJs in a specific region (Aird et al., 2022). By expanding the target domain to the whole of North America and revealing the climatological characteristics of LLJs in different regions and scales, this paper provides an accurate reference for future research on LLJ-related processes in North America.

The convection-permitting WRF model is able to recapture some LLJs that have been previously studied, such as the Great Plain S-LLJ and the California coastal N-LLJ in the eastern Pacific Ocean and has obtained relatively consistent results. The results indicate that the S-LLJ in the central US Plain is the most frequent and active in warm seasons and that three critical high-frequency centers occur in summer: the northeast Mexico-Texas border, west-central Texas, and western Oklahoma to southern Kansas. This last result is consistent with the climatology generated by Doubler et al. (2015) using the NARR reanalysis data, but the patterns here are more representative of the topographic features in central and southern Texas. In addition, compared with the 40-year rawinsonde climatology in the central US by Walters et al. (2008), our study reveals that the S-LLJ frequency range of these three centers in the central US in summer is 25%-30%, which is slightly lower than the 35% reported in the 2008 study. However, given the underestimated frequencies of 15%-20% in NARR climatology, there is an advantage of using high-resolution simulations in the vertical direction. Even though the simulation period does not match the time range of the literature exactly, the characteristics transcend specific time frames still offer a reference.

488   The convection-permitting simulation can also capture LLJs that were poorly detected previously using coarser

489   resolution models and observational datasets. The winter N-LLJs over the eastern Rocky Mountains described in this

490   paper are generally distributed over the central US from the Dakotas to Oklahoma with a low frequency (>10%) and

491   over several sporadic small areas with a high frequency (>20%) along the boundary of the Rockies. The main

492   seasonal/diurnal variations identified in this study agree with those seen using rawinsonde data (Walters et al., 2008)

493   and NARR reanalysis (Douber et al., 2015). But the frequency of the LLJ occurrence over Nebraska-Kansas was

494   underestimated in both convection-permitting simulations (~10%) and NARR (~7%), while high-frequency hot spots

495   from Alberta to Colorado were not detected in either of the above-mentioned studies, probably because measurements

496   are lacking in these regions. The high-resolution simulation also detected LLJs on which researchers have hardly

497   focused: N-LLJs near the eastern Quebec coast and in the Appalachians Mountains, as well as an S-LLJ over the

498   British Columbia coast. In the work of Douber et al. (2015), these LLJs were shown in the climatology patterns, but

499   the 4-km WRF simulation offered more detailed descriptions of their locations. For example, this study found that the

500   Appalachian N-LLJ extends from Georgia to the northwestern Atlantic, especially on summer nights (03 UTC – 06

501   UTC), while NARR only captured LLJ occurrences over the middle coast of the Atlantic. The maximum frequency

502   (7-10%) detected in the NARR study is also less than what is illustrated here. As for the Quebec N-LLJ, the 4-km

503   WRF revealed that it mostly occurs onshore near the coast with a frequency of over 25% in winter, but NARR only

504   provided a coarse occurrence distribution over northeastern Canada.

505   Based on the inertial oscillation theory (Blackadar, 1957) and the baroclinic theory near complex terrain (Holton,

506   1967), this paper also analyzed the background and formation mechanisms of three LLJs: the Great Plain S-LLJ,

507   Quebec N-LLJ, and California coastal N-LLJ. Generally, all these LLJs are impacted by the thermodynamic

508   circulations generated near their topography. The Great Plain S-LLJ is affected by slope heating, and the LLJs over

509   Quebec and California are associated with the sea-land contrast. When the geostrophic and ageostrophic components

510   of the LLJs are compared, results show that the inertial oscillation better explains the night enhancement of the Great

511   Plains S-LLJ and that the diurnal feature of the Quebec N-LLJ is influenced by the combination of the Holton and

512   Blackadar theories. As for the California coastal N-LLJ, no supergeostrophic state is found, making coastal

513   baroclinicity variation a dominant factor for this LLJ's evolution the geostrophic wind changes.

514   This research adds to the existing knowledge of characteristics of the low-level wind maxima in North America, thus

515   helping researchers obtain more reliable references about LLJs in this domain. Meanwhile, with the high-resolution

516   features, it can provide more robust explanations for other interdisciplinary fields. The research also advances

517   knowledge about the formation of three dominant LLJs. Although the 13-year simulation is likely too short to provide

518   an ideal long-term climatic analysis, it is a less expensive option for finer numerical modelling in large domains.

519   Additionally, we acknowledge certain limitations in the convection-permitting WRF simulation. While the vertical

520   resolution in the boundary layer of this simulation is enhanced compared to other RCMs or reanalysis datasets, it

521   remains inferior to the observation density of radiosonde soundings. Consequently, the underestimation of LLJ events

522   in this paper is expected, as noted in previous comparative analyses. Furthermore, numerical models inherently possess

523   biases and uncertainties. Although employing the convection-permitting scale mitigates some uncertainties, it is

524   important to recognize the limitations of these results. Additionally, the version of the input dataset used in this

525   research is obsolete. However, with future advancements in technology, it is expected that longer and more accurate

526   high-resolution simulations, as well as newer input data like ERA5, will become available. Future work will address

527   the features and formation mechanisms of the small-scale low-level wind maxima, which have yet to be investigated.

528   **Acknowledgments**

529   All authors thank the support of the NSERC Discovery Grant and the NSERC Alliance the Northern Hail Project.

530

531   **Data Availability Statement**

532   The WRF simulation over CONUS can be accessed at Research Data Archive of NCAR

533   https://rda.ucar.edu/datasets/ds612.0/.

534

535   **Author contribution**

536   Xiao Ma: Conceptualization; data curation; formal analysis; investigation; methodology; visualization; writing-

537   original draft.

538   Yanping Li: Conceptualization; funding acquisition; investigation; methodology; project administration; supervision;

539   validation; writing-review and editing.

540   Zhenhua Li: Data curation; methodology; validation; visualization; writing-review and editing.

541   Fei Huo: Data curation; methodology; validation; visualization; writing-review and editing.

542

543   **Competing interests**

544   All authors disclosed no relevant relationships.

545

Appendix

Winter LLJs captured by ERA5 Dataset

The convection-permitting WRF simulation exhibited excellent performance in investigating well-known LLJ systems, such as the California coastal N-LLJ and the Great Plains S-LLJ. Moreover, this appendix validates WRF-simulated significant winter jet systems over North America using the ERA5 reanalysis dataset. ERA5 is a global atmospheric reanalysis dataset produced by the European Centre for Medium-Range Weather Forecasts (ECMWF). It provides hourly data on a horizontal grid space of approximately 31 km, and the time range covers from 1979 till the present. ERA5 data is widely used in climate research, weather forecasting, and various applications that require high-quality atmospheric data.

The validation period is the same as the WRF simulation (2000-2013). From the Figure A1 below, it is evident that during winter, a greater number of significant N-LLJ systems in the North American continent are mostly concentrated in eastern Canada. In most parts of Newfoundland and southeastern Quebec, the occurrence frequency of N-LLJs exceeds 15%, and the maximum can even surpass 25%. However, in the WRF simulation (Figure 3d), the model can only capture N-LLJs on the north bank of the St. Lawrence River due to the northern boundary of the study domain overlapping with the Quebec border. In comparison, the WRF-simulated frequency of N-LLJs in southeastern Quebec essentially exceeds 25%, overestimated by about 5% compared to the ERA5 reanalysis. Additionally, it is worth noting that the N-LLJs along the downstream of Rockies are also identified in the ERA5 dataset. The areas where the frequency exceeds 5% are mainly distributed from Alberta to northern Texas, consistent with the findings in Section 3.2.1. Moreover, the high-value center (>10%) is located in central Kansas. In terms of the differences between the two datasets, the results of the WRF simulation match more geographical features and reveal scattered high-value spots (>15%) in some regions with special terrains (see Figure 3d). Furthermore, the winter Great Plains S-LLJs in ERA5 reanalysis exhibit similar features, with frequencies ranging from around 15% to 20% in southern Texas. In summary, the WRF model can accurately capture the features of winter LLJ systems, which are validated by the ERA5 reanalysis dataset over northern America. Even though the frequency of LLJs occurrence is overestimated, the convection-permitting WRF simulation can provide detailed descriptions of LLJs near complex terrains.

571
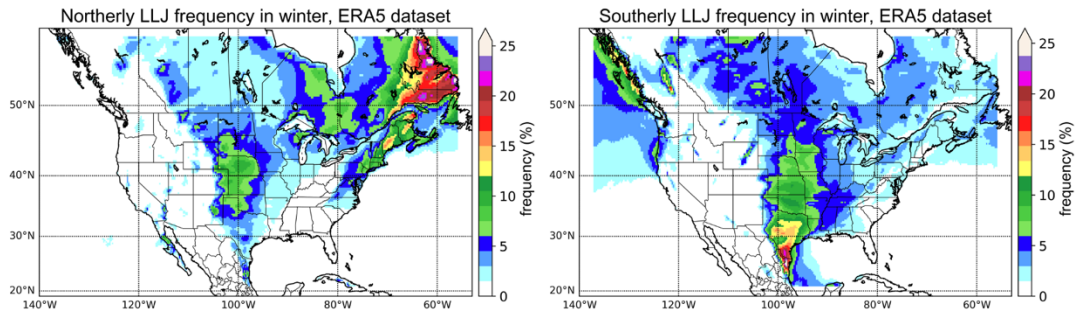
Figure A1. Winter occurrence frequency of N-LLJs (left) and S-LLJs (right).

573

574

575

Data Availability Statement

577   The ERA5 dataset is available on the Copernicus Climate Change Service Information website.

578   https://cds.climate.copernicus.eu/#!/home

579
580

References

Aird, J. A., Barthelmie, R. J., Shepherd, T. J. and Pryor, S. C.: Occurrence of Low-Level Jets over the Eastern U.S. Coastal Zone at Heights Relevant to Wind Energy, Energies, 15(2), 445, doi:10.3390/en15020445, 2022.

Blackadar, A. K.: Boundary Layer Wind Maxima and Their Significance for the Growth of Nocturnal Inversions, Bulletin of the American Meteorological Society, 38(5), 283–290, doi:10.1175/1520-0477-38.5.283, 1957.

Bonner, W. D.: CLIMATOLOGY OF THE LOW LEVEL JET, Monthly Weather Review, 96(12), 833–850, doi:10.1175/1520-0493(1968)096<0833:cotllj>2.0.co;2, 1968.

Chen, G. T.-J., Wang, C.-C. and Lin, D. T.-W.: Characteristics of Low-Level Jets over Northern Taiwan in Mei-Yu Season and Their Relationship to Heavy Rain Events, Monthly Weather Review, 133(1), 20–43, doi:10.1175/mwr-2813.1, 2005.

Doubler, D. L., Winkler, J. A., Bian, X., Walters, C. K. and Zhong, S.: An NARR-Derived Climatology of Southerly and Northerly Low-Level Jets over North America and Coastal Environs, Journal of Applied Meteorology and Climatology, 54(7), 1596–1619, doi:10.1175/jamc-d-14-0311.1, 2015.

Du, Y. and Chen, G.: Heavy Rainfall Associated with Double Low-Level Jets over Southern China. Part II: Convection Initiation, Monthly Weather Review, 147(2), 543–565, doi:10.1175/mwr-d-18-0102.1, 2019.

Frisch, A. S., Orr, B. W. and Martner, B. E.: Doppler Radar Observations of the Development of a Boundary-Layer Nocturnal Jet, Monthly Weather Review, 120(1), 3–16, doi:10.1175/1520-0493(1992)120<0003:drootd>2.0.co;2, 1992.

Fu, P., Zhu, K., Zhao, K., Zhou, B. and Xue, M.: Role of the nocturnal low-level jet in the formation of the morning precipitation peak over the Dabie Mountains, Advances in Atmospheric Sciences, 36(1), 15–28, doi:10.1007/s00376-018-8095-5, 2018.

Gadde, S. N. and Stevens, R. J. A. M.: Effect of low-level jet height on wind farm performance, Journal of Renewable and Sustainable Energy, 13(1), 013305, doi:10.1063/5.0026232, 2021.

604   Hodges, D. and Pu, Z.: Characteristics and Variations of Low-Level Jets and Environmental Factors Associated with

605   Summer Precipitation Extremes over the Great Plains, Journal of Climate, 32(16), 5123–5144, doi:10.1175/jcli-d-18-

606   0553.1, 2019.

607   Hoffmann, L. and Spang, R.: An assessment of tropopause characteristics of the ERA5 and era-interim meteorological

608   reanalyses, Atmospheric Chemistry and Physics, 22(6), 4019–4046, doi:10.5194/acp-22-4019-2022, 2022.

609   Holton, J. R.: The diurnal boundary layer wind oscillation above sloping terrain, Tellus, 19(2), 199–205,

610   doi:10.1111/j.2153-3490.1967.tb01473.x, 1967.

611   Hong, S.-Y., Noh, Y. and Dudhia, J.: A New Vertical Diffusion Package with an Explicit Treatment of Entrainment

612   Processes, Monthly Weather Review, 134(9), 2318–2341, doi:10.1175/mwr3199.1, 2006.

613   Hu, X.-M., Klein, P. M., Xue, M., Lundquist, J. K., Zhang, F. and Qi, Y.: Impact of Low-Level Jets on the Nocturnal

614   Urban Heat Island Intensity in Oklahoma City, Journal of Applied Meteorology and Climatology, 52(8), 1779–1802,

615   doi:10.1175/jamc-d-12-0256.1, 2013.

616   Iacono, M. J., Delamere, J. S., Mlawer, E. J., Shephard, M. W., Clough, S. A. and Collins, W. D.: Radiative forcing

617   by long-lived greenhouse gases: Calculations with the AER radiative transfer models, Journal of Geophysical

618   Research, 113(D13), doi:10.1029/2008jd009944, 2008.

619   Jain, P. and Flannigan, M.: The relationship between the Polar Jet Stream and extreme wildfire events in North

620   America, Journal of Climate, 1–59, doi:10.1175/jcli-d-20-0863.1, 2021.

621   Jiménez-Sánchez, G., Markowski, P. M., Jewtoukoff, V., Young, G. S. and Stensrud, D. J.: The Orinoco Low-Level

622   Jet: An Investigation of Its Characteristics and Evolution Using the WRF Model, Journal of Geophysical Research:

623   Atmospheres, 124(20), 10696–10711, doi:10.1029/2019jd030934, 2019.

624   Kurkute, S., Li, Z., Li, Y. and Huo, F.: Assessment and projection of the water budget over Western Canada using

625   convection-permitting weather research and forecasting simulations, Hydrology and Earth System Sciences, 24(7),

626   3677–3697, doi:10.5194/hess-24-3677-2020, 2020.

627   Li, Y., Li, Z., Zhang, Z., Chen, L., Kurkute, S., Scaff, L. and Pan, X.: High-resolution regional climate modeling and

628   projection over Western Canada using a weather research forecasting model with a pseudo-global warming approach,

629   Hydrology and Earth System Sciences, 23(11), 4635–4659, doi:10.5194/hess-23-4635-2019, 2019.

630   Lin, Y., Wang, C., Yan, J., Li, J. and He, S.: Observation and simulation of low-level jet impacts on 3D urban heat

631   islands in Beijing: A case study, Journal of the Atmospheric Sciences, 79(8), 2059–2073, doi:10.1175/jas-d-21-0245.1,

632   2022.

633   Liu, C., Ikeda, K., Rasmussen, R., Barlage, M., Newman, A. J., Prein, A. F., Chen, F., Chen, L., Clark, M., Dai, A.,

634   Dudhia, J., Eidhammer, T., Gochis, D., Gutmann, E., Kurkute, S., Li, Y., Thompson, G. and Yates, D.: Continental-

635   scale convection-permitting modeling of the current and future climate of North America, Climate Dynamics, 49(1–

636   2), 71–95, doi:10.1007/s00382-016-3327-9, 2016.

637   Ma, X., Li, Y. and Li, Z.: The projection of Canadian wind energy potential in future scenarios using a convection-

638   permitting regional climate model, Energy Reports, 8, 7176–7187, doi:10.1016/j.egyr.2022.05.122, 2022.

639   Miao, Y., Guo, J., Liu, S., Wei, W., Zhang, G., Lin, Y., Zhai, P., Zhai, P., Lin, Y., Zhang, G., Wei, W., Liu, S., Guo,

640   J. and Miao, Y.: The Climatology of Low-Level Jet in Beijing and Guangzhou, China, Journal of Geophysical

641   Research: Atmosphere, 123(5), 2816–2830, doi:10.1002/2017jd027321, 2018.

642   Mitchell, M. J., Arritt, R. W. and Labas, K.: A Climatology of the Warm Season Great Plains Low-Level Jet Using

643   Wind   Profiler   Observations,   Weather   and   Forecasting,   10(3),   576–591,   doi:10.1175/1520-

644   0434(1995)010<0576:acotws>2.0.co;2, 1995.

645   Montini, T. L., Jones, C. and Carvalho, L. M. V.: The South American Low-Level Jet: A New Climatology, Variability,

646   and Changes, Journal of Geophysical Research: Atmospheres, 124(3), 1200–1218, doi:10.1029/2018jd029634, 2019.

647   Munday, C., Washington, R. and Hart, N.: African Low-Level Jets and Their Importance for Water Vapor Transport

648   and Rainfall, Geophysical Research Letters, 48(1), doi:10.1029/2020gl090999, 2021.

649 Niu, G.-Y., Yang, Z.-L., Mitchell, K. E., Chen, F., Ek, M. B., Barlage, M., Kumar, A., Manning, K., Niyogi, D.,

650 Rosero, E., Tewari, M. and Xia, Y.: The community Noah land surface model with multiparameterization options

651 (Noah-MP): 1. Model description and evaluation with local-scale measurements, Journal of Geophysical Research,

652 116(D12), doi:10.1029/2010jd015139, 2011.

653 Parish, T. R.: Forcing of the Summertime Low-Level Jet along the California Coast, Journal of Applied Meteorology,

654 39(12), 2421–2433, doi:10.1175/1520-0450(2000)039<2421:fotsll>2.0.co;2, 2000.

655 Pu, B. and Cook, K. H.: Dynamics of the West African westerly jet, Journal of Climate, 23(23), 6263–6276,

656 doi:10.1175/2010jcli3648.1, 2010.

657 Rahn, D. A. and Parish, T. R.: Diagnosis of the Forcing and Structure of the Coastal Jet near Cape Mendocino Using

658 In Situ Observations and Numerical Simulations, Journal of Applied Meteorology and Climatology, 46(9), 1455–1468,

659 doi:10.1175/jam2546.1, 2007.

660 Rife, D. L., Pinto, J. O., Monaghan, A. J., Davis, C. A. and Hannan, J. R.: Global Distribution and Characteristics of

661 Diurnally Varying Low-Level Jets, Journal of Climate, 23(19), 5041–5064, doi:10.1175/2010jcli3514.1, 2010.

662 Saulo, C., Ruiz, J. and Skabar, Y. G.: Synergism between the Low-Level Jet and Organized Convection at Its Exit

663 Region, Monthly Weather Review, 135(4), 1310–1326, doi:10.1175/mwr3317.1, 2007.

664 Shapiro, A., Fedorovich, E. and Rahimi, S.: A unified theory for the Great Plains Nocturnal low-level jet, Journal of

665 the Atmospheric Sciences, 73(8), 3037–3057, doi:10.1175/jas-d-15-0307.1, 2016.

666 Smith, E. N., Gebauer, J. G., Klein, P. M., Fedorovich, E. and Gibbs, J. A.: The Great Plains Low-Level Jet during

667 PECAN: Observed and Simulated Characteristics, Monthly Weather Review, 147(6), 1845–1869, doi:10.1175/mwr-

668 d-18-0293.1, 2019.

669 Soares, P. M., Lima, D. C., Semedo, A., Cardoso, R. M., Cabos, W. and Sein, D. V.: Assessing the climate change

670 impact on the North African offshore surface wind and coastal low-level jet using coupled and uncoupled regional

671 climate simulations, Climate Dynamics, 52(11), 7111–7132, doi:10.1007/s00382-018-4565-9, 2018.

672   Stensrud, D. J.: Importance of Low-Level Jets to Climate: A Review, Journal of Climate, 9(8), 1698–1711,

673   doi:10.1175/1520-0442(1996)009<1698:iolljt>2.0.co;2, 1996.

674   Sullivan, J. T., Rabenhorst, S. D., Dreessen, J., McGee, T. J., Delgado, R., Twigg, L. and Sumnicht, G.: Lidar

675   observations revealing transport of O3 in the presence of a nocturnal low-level jet: Regional implications for "next-

676   day" pollution, Atmospheric Environment, 158, 160–171, doi:10.1016/j.atmosenv.2017.03.039, 2017.

677   Tang, Y., Winkler, J., Zhong, S., Bian, X., Doubler, D., Yu, L. and Walters, C.: Future changes in the climatology of

678   the Great Plains low-level jet derived from fine resolution multi-model simulations, Scientific Reports, 7(1),

679   doi:10.1038/s41598-017-05135-0, 2017.

680   Uccellini, L. W., Petersen, R. A., Kocin, P. J., Brill, K. F. and Tuccillo, J. J.: Synergistic Interactions between an

681   Upper-Level Jet Streak and Diabatic Processes that Influence the Development of a Low-Level Jet and a Secondary

682   Coastal Cyclone, Monthly Weather Review, 115(10), 2227–2261, doi:10.1175/1520-

683   0493(1987)115<2227:sibaul>2.0.co;2, 1987.

684   Van de Wiel, B. J., Moene, A. F., Steeneveld, G. J., Baas, P., Bosveld, F. C. and Holtslag, A. A.: A conceptual view

685   on inertial oscillations and nocturnal low-level jets, Journal of the Atmospheric Sciences, 67(8), 2679–2689,

686   doi:10.1175/2010jas3289.1, 2010.

687   Walters, C. K. and Winkler, J. A.: Airflow Configurations of Warm Season Southerly Low-Level Wind Maxima in

688   the Great Plains. Part I: Spatial and Temporal Characteristics and Relationship to Convection, Weather and

689   Forecasting, 16(5), 513–530, doi:10.1175/1520-0434(2001)016<0513:acowss>2.0.co;2, 2001.

690   Walters, C. K., Winkler, J. A., Shadbolt, R. P., van Ravensway, J. and Bierly, G. D.: A Long-Term Climatology of

691   Southerly and Northerly Low-Level Jets for the Central United States, Annals of the Association of American

692   Geographers, 98(3), 521–552, doi:10.1080/00045600802046387, 2008.

693   Weide Luiz, E. and Fiedler, S.: Spatiotemporal observations of nocturnal low-level jets and impacts on wind

694   power production, Wind Energy Science, 7(4), 1575–1591, doi:10.5194/wes-7-1575-2022, 2022.

695   Zhang, Y., Xue, M., Zhu, K. and Zhou, B.: What is the main cause of diurnal variation and nocturnal peak of summer

696   precipitation in Sichuan Basin, China? the key role of boundary layer low-level jet inertial oscillations, Journal of

697   Geophysical Research: Atmospheres, 124(5), 2643–2664, doi:10.1029/2018jd029834, 2019.

698   Zhong, S., Fast, J. D. and Bian, X.: A Case Study of the Great Plains Low-Level Jet Using Wind Profiler Network

699   Data and a High-Resolution Mesoscale Model, Monthly Weather Review, 124(5), 785–806, doi:10.1175/1520-

700   0493(1996)124<0785:acsotg>2.0.co;2, 1996.